A low-temperature glide cycle for pumped thermal energy storage†

Antoine Koen[a], Pau Farres-Antunez[a], James Macnaghten[b], Alexander White*,[a]
[a]*University of Cambridge, Engineering Department, Trumpington Street, Cambridge, CB2 1PZ, United Kingdom*
[b]*Caldera Heat Batteries Ltd, United Kingdom*
**Corresponding author. Email address: ajw36@cam.ac.uk*

Abstract

Pumped thermal energy storage is seen as a possible alternative to pumped-hydro schemes for storing electricity at large scale and facilitating increased integration of renewable sources. This paper presents a novel form of pumped thermal energy storage in which the thermodynamic cycle exploits the temperature glide exhibited by zeotropic mixtures. The working fluid is a blend of linear alkanes, optimised so as to obtain a near-constant effective heat capacity in the two-phase region. This enables heat exchange with the storage fluid in a manner that incurs very low exergetic losses whilst also achieving a high cycle work ratio. These two features allow the cycle to attain a respectable round-trip efficiency whilst operating at low temperature (0–100 °C). The analysis presented constitutes a preliminary thermodynamic design; further improvements to performance may be possible with comprehensive optimisation. Nonetheless, the results show that an overall (electricity-to-electricity) round-trip efficiency of around 50% should be achievable with unpressurised water as the storage fluid. Initial cost estimates have also been undertaken, showing marginal energy (capital) costs in the range 15–45 $\$/\mathrm{kWh_e}$, depending on the type of containment. Due to the low power density and high heat-to-work ratio of low-temperature storage, the estimated marginal capital cost per unit power capacity is less favourable (1,300–2,900$\$/\mathrm{kW}$) implying the system is best-suited to long-duration discharge.

† The published article is available here (unrestricted) until 01 October 2021, and subsequently here (restricted).

Index Terms

pumped thermal energy storage, zeotropic mixtures, temperature glide, Kalina cycle

1. Introduction

1.1 Context

With the urgent need to reduce greenhouse gas emissions from fossil fuels, the world is turning to low-carbon sources of energy. Renewable forms of electricity in particular have been growing rapidly, spurred on by the falling cost of wind turbines and solar photovoltaic cells [1]. These forms of generation are now competitive with (if not cheaper than) conventional, fossil-fuel generation [2] but they are well-known for being intermittent and non-dispatchable. For example, the current installed capacity of wind generation in the UK is approximately 25 GW, with a capacity factor that varies from year to year but is in the range 30 to 35% [3]. However, according to data available from Ref. [4], there were 10 occasions in 2020 when output fell below 25% of its *average* value (i.e., 8% of capacity) for a duration of 2 days or more. Such variability is currently managed by load-following plant such as combined-cycle gas turbines, but it is evident that energy storage, along with demand-side management, is likely to play a much greater role as we move towards a carbon-free future. It is not surprising, therefore, that many new energy storage technologies have been proposed or are under development, ranging from short time-scale, high power-density devices such as flywheels and supercapacitors, through medium-term storage (e.g., compressed air energy storage – CAES – and liquid air energy storage – LAES) and ultimately to solutions suitable for inter-seasonal storage such as synthetic fuels (see for example [5]).

The present paper describes a novel form of pumped thermal energy storage (PTES) based on a cycle similar to the Kalina cycle [6]. The aim is to combine the benefits of high "work ratio" (see below) exhibited by Rankine-based cycles with the ease of integration with sensible heat storage, the latter being a feature of Joule-Brayton PTES systems in particular. The results suggest that such a system can achieve an acceptable round-trip efficiency whilst using unpressurised water as the storage medium. This offers the advantages of rapid start-up times and low marginal capital cost per kWh storage capacity, and avoids the need for expensive, exotic materials. From an economic perspective, such a system is aimed at the longer-duration shortfalls discussed above, which would be prohibitively expensive to cover using batteries.

1.2 Pumped Thermal Energy Storage

Pumped thermal energy storage (which also goes by other names, including the "Carnot Battery" and "Pumped Heat Storage") is now a reasonably well-established thermo-mechanical storage concept. Several schemes have been (or are currently) under commercial development, including Isentropic's pumped heat system in the UK [7] and the Malta project in the US [8]. The principle of operation is illustrated in fig. 1: during charge a quantity of electrical work W_{chg} is used to drive some form of

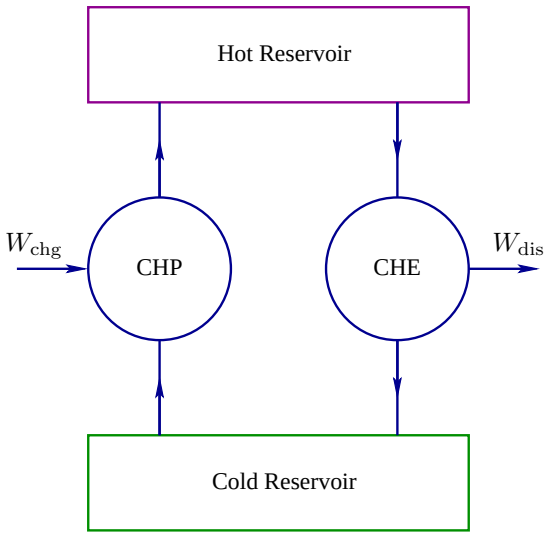

Fig. 1: Schematic diagram of generic PTES. (CHP = cyclic heat pump; CHE = cyclic heat engine.)

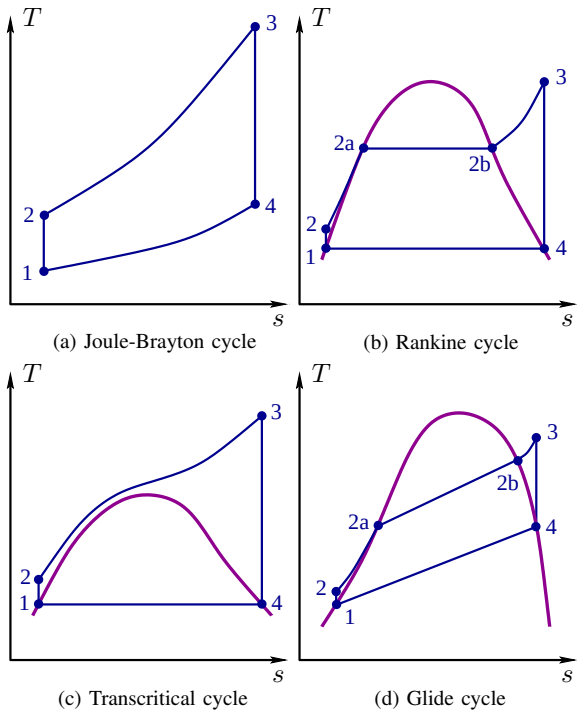

Fig. 2: *T*-*s* sketches for different PTES cycles. The order of states applies to the discharge (heat engine) phase.

cyclic heat pump (CHP), thereby transferring heat from a cold to a hot thermal reservoir. The energy flows are reversed during discharge via a cyclic heat engine (CHE), returning work W_{dis}. The concept is analogous to pumped-hydro storage, but with heat rather than water being pumped, and thermal energy rather than gravitational potential energy being stored. In common with pumped-hydro storage (but in contrast to most electrochemical batteries), the energy and power capacities of PTES are easily decoupled by adjusting the relative size of the reservoirs and power-conversion machinery.

Many different embodiments of PTES have been proposed, based on a variety of storage media (solid/liquid, latent/sensible heat) using different thermodynamic cycles and with a range of working fluids. *T*-*s* diagrams for the main heat pump/engine cycles studied so far are depicted in fig. 2(a-c). Joule-Brayton-based PTES operates with a near-ideal gas (e.g, argon or nitrogen) as the working fluid and pairs very well with sensible-heat storage due to the essentially constant heat capacity of such gases. It requires both hot and cold stores, the latter usually being at substantially sub-ambient temperatures. By contrast, both Rankine [9] and transcritical systems [10] can dispense with the cold reservoir by exchanging heat with the atmosphere during the cold isothermal process (states 4 to 1 in fig. 2b and 2c). This has the advantage of achieving higher energy density (for a given temperature range), but practical difficulties associated with ice formation, especially during charge, may need to be dealt with

in some climates.

The rationale behind the transcritical cycle is that it (partially) alleviates pinch-point problems that would otherwise occur with a Rankine cycle when operating in conjunction with sensible-heat storage. There is particular interest in transcritical CO_2 cycles due to their high power density (e.g., [10]) but other candidate working fluids have been explored by Koen *et al* [11].

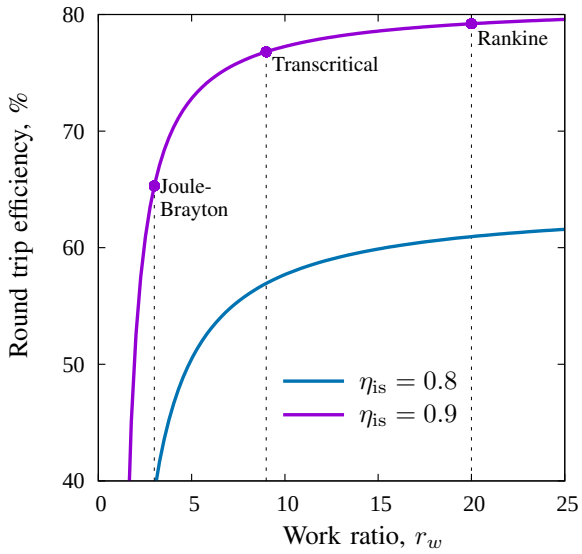

Fig. 3: Approximate maximum round-trip efficiency given by eq.(1). Typical work ratios for the different cycles are: Joule-Brayton 2-4 [12]; transcritical ~ 9 [11]; Rankine > 20 [12].

An important quantity in determining the performance of each of the above cycles is their work ratio, r_w, defined for a heat engine as the ratio of expansion to compression work (or *vice versa* for a heat pump). The net work transfer is the difference between these two work terms, so if r_w is close to unity the net work becomes very sensitive to irreversibility in the compressors and expanders. This effect may be quantified by the following approximate expression for round-trip efficiency for PTES systems (see [13]), applicable when compression and expansion losses dominate:

$$\eta_{RT} \simeq \frac{r_w - 1/\eta_{\rm is}^2}{r_w/\eta_{\rm is}^2 - 1} < \eta_{\rm is}^2 \tag{1}$$

where $\eta_{\rm is}$ is the isentropic efficiency, assumed equal for all compressors and expanders. This expression is plotted in fig. 3 for isentropic efficiencies of 80 and 90%. The inherently low work ratio of the the Joule-Brayton cycle means that high-efficiency turbomachinery is required to obtain a respectable round-trip efficiency. Improvements to its work ratio can be achieved by recuperation (see, for example, Ref. [14]) but at the expense of greater complexity and additional heat-transfer loss. By contrast, the Rankine and transcritical cycles have significantly higher work ratios because the "compression" process (states 1 to 2 in fig. 2) occurs in the high-density liquid phase. For these cycles eq.(1) approaches its maximum value of $\eta_{\rm is}^2$ and $\eta_{\rm RT}$ is relatively insensitive to feed-pump losses. The corresponding expansion process during the charging (heat-pump) phase can therefore be accomplished via a throttle without significant penalty.

1.3 The glide-cycle PTES

The high work ratio of the transcritical and Rankine cycles comes at the expense of less facility for integration with sensible-heat storage. This is particularly evident in the Rankine-based system, for which the liquid-vapour phase change would be most conveniently paired with latent-heat storage. For the transcritical cycle, unless very highly supercritical pressures are employed, the working fluid exhibits significant variations in specific heat capacity between states 2 and 3, giving rise to heat-transfer pinch points. These difficulties provide the motivation for the present investigation of a "glide cycle", similar to the Kalina cycle.

The Kalina cycle is essentially a modified Rankine cycle in which the working fluid is a mixture of two or more components. By virtue of compositional variations, evaporation and condensation thus occur non-isothermally, exhibiting instead temperature "glide", as shown in processes 2a to 2b and 4 to 1 in fig. 2d. As a result, the glide-based system enjoys high work ratio whilst also coupling easily and efficiently with sensible-heat storage. (The potential pinch-point problem at state 2a is readily avoided, as described in section 2.) Most of the existing literature for Kalina cycles focuses on electricity production from low-grade heat, such as geothermal sources [15] or waste-heat recovery [16], [17]. Results indicate that higher exergetic efficiencies are achieved than with comparable organic Rankine cycles (ORCs) [6], but a disadvantage is that evaporator and condenser

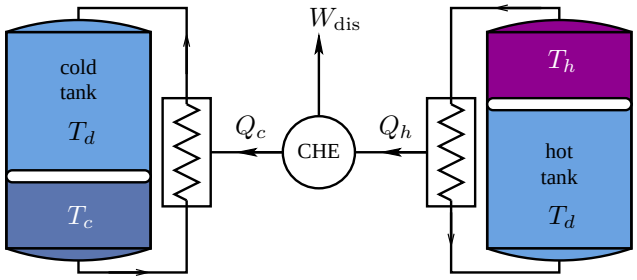

Fig. 4: Idealised hot-and-cold PTES during discharge

costs are likely to be higher, due to lower heat transfer coefficients compared with pure fluids [17]. Temperature glide is also exploited in the HVAC and refrigeration industries, where blended refrigerants (e.g., R-354C) are now quite common.

In the context of energy storage, the use of glide-based cycles has recently been proposed for heat recovery from LAES and CAES systems. Zhang *et al* [18], for example, predict a 5 percentage point increase in round-trip efficiency (from 52% to 57%) over their baseline LAES system by employing a Kalina cycle to exploit low-temperature "compression heat". On the other hand, Soltani *et al* [19] compare Kalina cycles with ORCs (the latter using a variety of single-component working fluids) for "waste-heat" recovery from a CAES system, but conclude that the supercritical ORC performs best. In both these examples, however, the Kalina cycle uses a binary ammonia-water mixture as the working fluid which, as shown in section 2, is unlikely to provide highly efficient heat exchange. More generally, several authors have studied the choice and molar composition of zeotropic mixtures (i.e., ones that give temperature glide) in terms of impact on thermodynamic cycle performance. Examples are given in Refs. [20]–[22], all of which consider only binary mixtures, with a focus on obtaining the appropriate glide range. An important observation from this work (see in particular Ref. [20]) is that blending "wet" and "dry" fluids enables control over the slope of the vapour saturation line on the *T-s* diagram, with implications for operation of the turbine and/or use of internal recuperation. Variations of the effective specific heat capacity in the two-phase region have not, however, been fully explored.

The original contribution of the present work is firstly that a glide-based cycle is proposed as the *primary* thermodynamic cycle for a PTES system. This has not appeared elsewhere in the literature and is in contrast to the work presented in Refs. [18] and [19] where the Kalina cycles have a secondary function as heat recovery cycles. Secondly, the working fluid proposed here is a four-component mixture whose composition is carefully tailored to achieve near-constant heat capacity. As discussed in section 2, this is necessary to provide exergetically efficient heat exchange with the storage fluid and is particularly important for low-temperature storage.

2. Storage density and system layout

2.1 Maximum storage density

Since temperature glide occurs during both evaporation and condensation (see fig. 2d), it is evident that a glide-based PTES system will require both hot and cold storage. The present study is confined to using unpressurised water as the storage medium, and it is therefore instructive to consider the maximum energy density that can be achieved with such a system (i.e., one that does not use the environment as a heat source or sink). This serves as a useful benchmark for real systems, and guides the choice of cycle temperatures.

Figure 4 shows an idealised PTES arrangement during its discharge phase, wherein a mass m_h of water in the hot tank is cooled from its top temperature T_h to an intermediate "discharged" temperature T_d, whilst m_c in the cold tank is heated from T_c (the minimum temperature) to T_d. (Note that the discharged state of the two tanks must be at the same temperature, otherwise additional work could be extracted.) The corresponding heat transfers Q_h and Q_c drive a cyclic heat engine (CHE) which delivers work W_{dis}. The energy density (work discharged per unit storage volume) is given by

$$\rho_E = \rho_w c_{pw}\{f(T_h - T_d) + (1-f)(T_c - T_d)\} \tag{2}$$

where $f = m_h/(m_h + m_c)$, and ρ_w and c_{pw} are the density and isobaric specific heat capacity respectively of water (both assumed constant). The maximum work will be extracted under reversible conditions and (since the system as a whole must be adiabatic) the optimum storage density is thus given by maximising ρ_E at constant system entropy. The analysis is straightforward (see the Appendix) and leads to:

$$T_d^* = \frac{T_h - T_c}{\ln(T_h/T_c)} \tag{3}$$

and

$$f^* = \frac{\ln(T_d^*/T_c)}{\ln(T_h/T_c)} \tag{4}$$

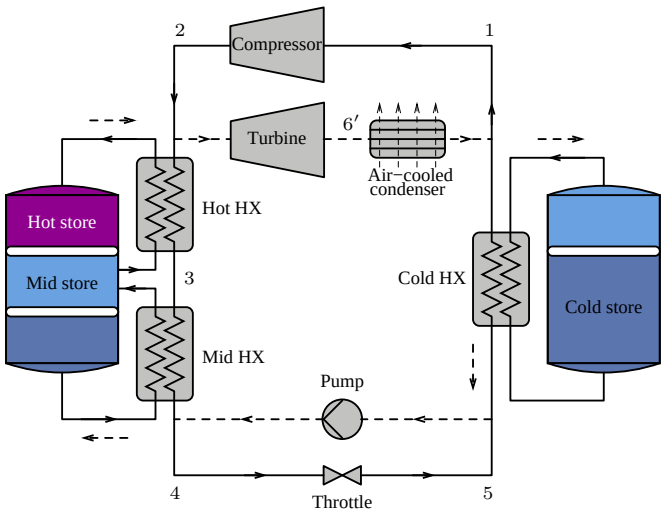

Fig. 5: Layout of the baseline glide PTES system. Solid lines denote charge and dashed lines discharge.

where the asterisk denotes the optimum value. In passing, it is worth noting that these expressions have a straightforward thermodynamic interpretation: T_d^* is the temperature of a fictitious environment at which the hot and cold stores would have the same *exergy* density, and f^* is then the unique mass distribution between the tanks that gives no heat transfer with that environment. In practice, f^* lies close to an even 50/50 split (see Appendix) for all realistic temperature ranges, such that T_d^* is approximately the geometric mean, $(T_h T_c)^{1/2}$.

Substituting values for water (assuming $T_c = 4\,^\circ\mathrm{C}$ – the maximum density point – and $T_h = 96\,^\circ\mathrm{C}$) gives a maximum energy density of $3.8\,\mathrm{kWh_e/m^3}$ with $T_d^* \simeq 48\,^\circ\mathrm{C}$ and $f^* \simeq 51\%$. Although this is a relatively low energy density compared to, for example, electrochemical batteries (for which ρ_E is typically several hundred $\mathrm{kWh_e/m^3}$) it is nonetheless substantially greater than that of pumped hydro schemes. Energy density and storage costs are discussed further in sections 2 and 1.

2.2 Layout of the glide PTES system

Figure 5 shows the layout and main components for one implementation of a glide-based PTES system. (Note the ordering of states corresponds to the charge cycle and is not consistent with fig. 2.) This constitutes the "baseline" configuration studied here; other arrangements are possible, as discussed below. The processes involved during the charge cycle are as follows:

a. Starting from a dry saturated state (point 1) at a temperature roughly midway between the hot and cold storage, the working fluid is first compressed adiabatically (but irreversibly) to achieve a temperature close to 100 °C (state 2).
b. It is then cooled and condensed to the wet saturated condition (state 3) whilst transferring heat to water in the hot tank.
c. It is further cooled to subcooled state 4, transferring heat to water in a mid-temperature store.
d. The subcooled liquid is isenthalpically throttled, entering the two-phase region (state 5).
e. The working fluid evaporates, returning to state 1, whilst absorbing heat from water in the cold tank.

These processes are essentially reversed during discharge – e.g., throttling is replaced by pumping and compression is replaced by expansion through the turbine. After the turbine expansion, heat is rejected to the environment (as required, since the round-trip efficiency is less than unity) via the air-cooled condenser. Further details of these processes are given below, including a plot of the cycles on the *T-s* diagram (fig. 8) and details of the fluid states (Table 1).

A notable difference between this system and the idealised system of fig. 4 is the additional "mid" heat exchanger on the hot side. This is required in order to alleviate the pinch-point problem that would otherwise occur at the wet-saturated condition (state 3); the specific heat capacity of the working fluid mixture is much lower in the liquid phase than in the two-phase region, so a commensurately lower mass flow of water is required in this intermediate heat exchanger.

Each store in fig. 5 has been shown schematically as a single tank in which the hot and cold fluids could be separated by stratification – i.e., the hotter, less dense fluid is at the top. This is an established approach commonly used in hot water storage, but temperature gradients will clearly decay over a period of time due to thermal conduction and (potentially) mixing. This can be mitigated by means of insulated separators (as shown in the figure) or by employing double-tank systems for each store. Alternatively, excavated pits can be used in place of tanks, as described in Refs. [23], [24].

3. Methods

3.1 Cycle calculations

The main analysis comprises standard thermodynamic cycle calculations in which compressors and expanders are treated as adiabatic and modelled with a specified isentropic efficiency. Similarly, a nominal temperature separation between streams,

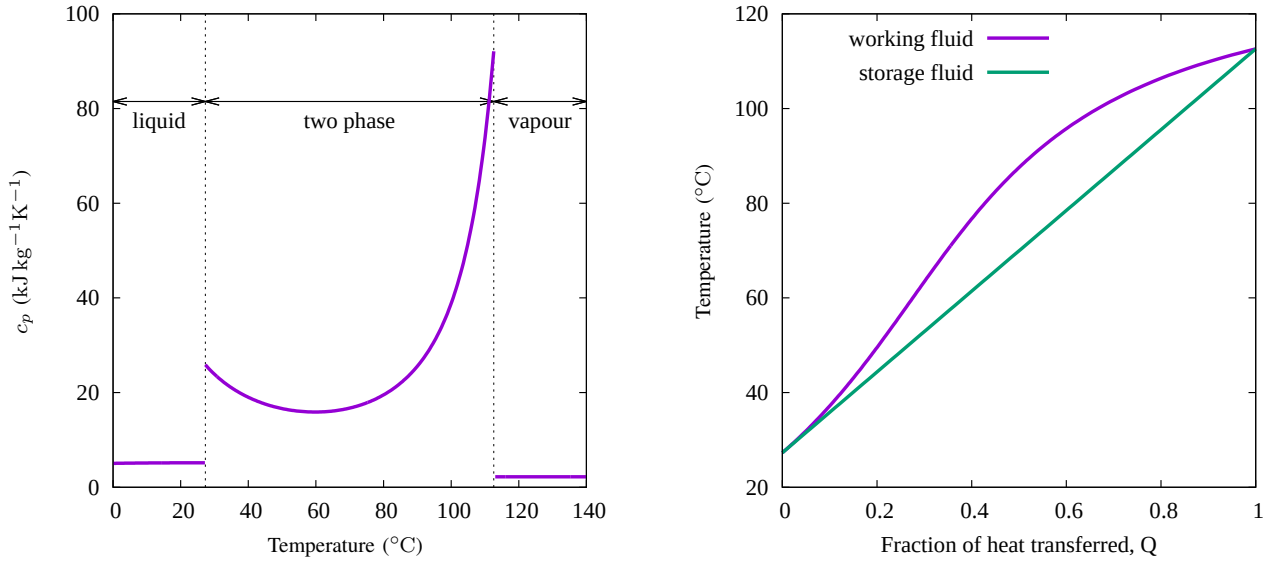

(a) Variation of c_p

(b) *T-Q* diagram

Fig. 6: Temperature glide for a 50-50 (molar) ammonia-water mixture at 3 bar: (a) c_p variation with temperature; (b) *T-Q* diagram for an infinite, counter-flow heat exchanger in the two-phase region with balanced average heat capacities.

ΔT, is specified for heat exchangers. As with several other initial studies of cycles (e.g., [9], [19], [20]) no pressure losses are considered at this stage, except in throttling processes. The Refprop library [25], widely recognised by academia and industry, is used to calculate fluid properties. All methods have been coded in Python by the authors.

3.2 Working fluid mixture optimisation

The original Kalina cycle employed an ammonia-water mixture with the advantages of safety and (due to the similar molecular weights of NH_3 and H_2O) properties sufficiently similar to those of water to exploit standard steam turbines [6]. Although such a mixture exhibits significant temperature glide, the variations of c_p within the two-phase region are very significant, as shown in fig. 6a. (Note that, in contrast to pure fluids, a two-phase c_p can be defined in the usual manner, namely $(\partial h/\partial T)_p$, due to the temperature glide.) These variations would result in very high heat-transfer irreversibility during any heat exchange between the working and storage fluids. This is evident in fig. 6b, which depicts the *T-Q* diagram for an infinite, counter-flow heat exchanger in which the average heat capacities of the two streams are balanced (i.e., $(\dot{m}c_p)_{\mathrm{sf}} = (\dot{m}\bar{c}_p)_{\mathrm{wf}}$) and the storage fluid has constant c_p. Although this heat exchanger has 100% effectiveness its exergetic efficiency (exergy delivered to storage fluid over exergy input from working fluid) is only 84%, as given by

$$\chi = \frac{\bar{c}_p(T_2 - T_1 - T_0 \ln\{T_2/T_1\})}{h_2 - h_1 - T_0(s_2 - s_1)} \tag{5}$$

where subscripts 1, 2 and 0 denote the cold end, hot end and environment respectively, and all properties are of the working fluid. It is evident that such a low exergetic efficiency would have a crippling impact on the performance of a storage system, given that a similar loss would be incurred during discharge.

The above example highlights one of the challenges inherent to low-temperature storage: small temperature separations during heat transfer entrain disproportionately large exergetic losses. This is essentially because the exergetic content of the heat transferred is so low (due to its low Carnot efficiency) and is reflected in a high heat-to-work ratio (HWR) of such systems, as discussed further below. Particular attention is therefore paid to the composition of the working fluid in order to minimise pinch-point related losses.

The present work focuses on blends of linear alkanes. Despite their obvious flammability, these offer several benefits including low cost, low global-warming and ozone-depletion potentials, and, thanks to extensive investigation by the oil and gas industries, they have well-documented properties. In particular, their binary interaction coefficients embedded within the Refprop database are deemed reliable [26]. By blending together several such alkanes it is possible to design a working fluid that has approximately the right glide but with only modest variations in c_p within the two-phase region. This is achieved by minimising the relative standard deviation (RSD $= \sigma/\bar{c}_p$, where σ is the standard deviation of c_p) for a mixture of ethane, propane, butane and pentane. The minimisation was carried out for three representative isobars using the sequential least-squares programming algorithm from Python's *SciPy* library.

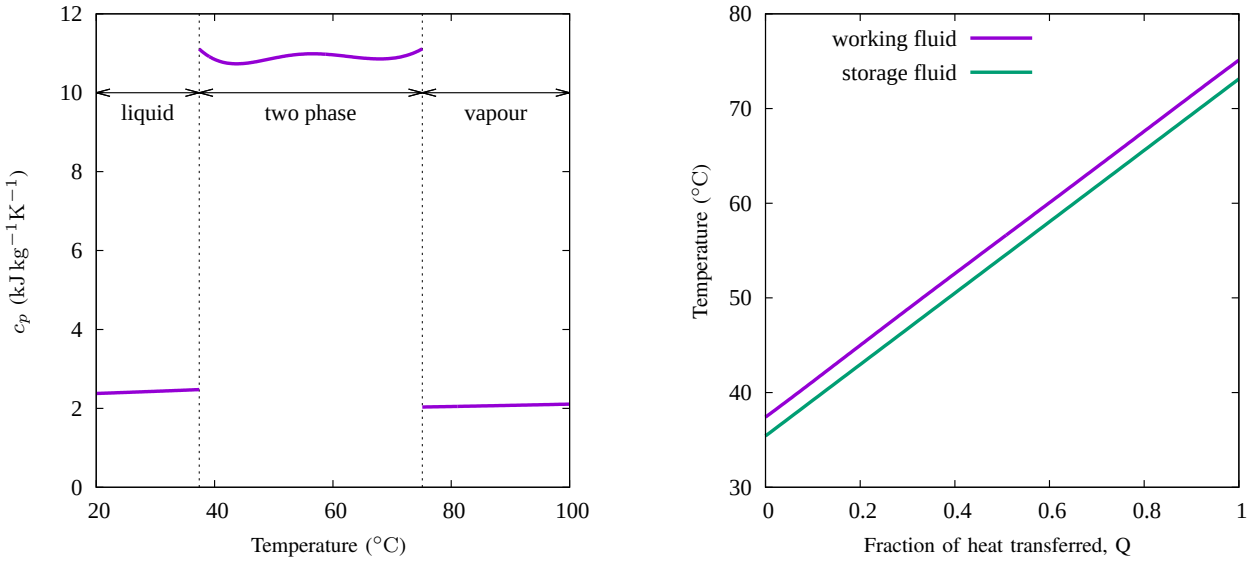

(a) Variation of c_p (b) *T-Q* diagram

Fig. 7: Temperature glide for a linear alkane mixture (C_3H_8 to C_6H_{14} in molar proportions 0.273/0.404/0.203/0.120) at 5 bar: (a) c_p variation with temperature; (b) *T-Q* diagram for a 95% effective, counter-flow heat exchanger in the two-phase region.

Figure 7 illustrates the outcome for one optimised blend (see caption in fig. 7 for composition) – the result is not unique because different bubble and dew point temperatures can be chosen. In this case the RSD c_p variation is just a few percent in the two-phase region, resulting in much more efficient heat exchange: the counter-flow process shown in fig. 7b has an effectiveness of 95% and attains an exergetic efficiency of 94%, despite the low temperature range.

4. Steady state analysis

The fully discharged state of the system comprises tanks of water at above-ambient temperature. An initial transient is therefore required to achieve this state but this is not considered in the results presented here, which focus instead on repeatable charge-discharge cycles.

4.1 Baseline configuration

Figure 8 shows the baseline cycle plotted on the *T-s* diagram, together with *T-Q* diagrams for the three heat exchangers (see layout in fig. 5). The compressor, pump and turbine each have a specified isentropic efficiency of 85% and the heat exchangers have a nominal 2 °C temperature difference ΔT, corresponding to an effectiveness of around 95%. Working fluid properties and tank temperatures for this baseline case are given in Tables 1 and 2 respectively. The working fluid molar composition is (0.096, 0.511, 0.201, 0.192) for the linear alkanes ethane to pentane respectively.

During charge the working fluid enters the compressor (state 1) as dry-saturated vapour and is compressed to approximately 100 °C, requiring a pressure ratio of 3.8. The particular blend of alkanes chosen gives a slightly "wet fluid" (i.e., the vapour saturation line is almost vertical, but with a negative slope) such that the compressor delivery (state 2) is slightly superheated. This creates a pinch point in the hot heat exchanger (top right of fig. 8b), but since only 3% of the heat is transferred in the superheated region the exergetic loss is small. As discussed above, the hot-side heat exchange is divided into two sections (processes 2 to 3 and 3 to 4 during charge) and it is notable that water is therefore simultaneously heated in the mid-temperature tank whilst being cooled in the cold tank over roughly the same temperature range. This serves as a form of recuperation which could alternatively be accomplished "internally" within the working fluid.

To avoid two-phase flow problems, the expansion during charge takes place via a throttle (process 4 to 5), and the corresponding pumping process during discharge occurs wholly in the liquid phase by ensuring state 5′ is at or very close to wet-saturated. Similarly, state 2′ is assumed dry-saturated to avoid damage to the turbine blades. This effectively sets the discharge pressure $p_{2'}$ and means that state 3′ (for the baseline case) is slightly subcooled liquid. Consequently, there is a second very minor pinch point in the hot heat exchanger during discharge, which is just evident in the bottom left of fig. 8b. The other heat exchangers have near-parallel *T-Q* profiles (fig. 8c-d), with only small deviations due to slight variations in c_p of the working fluid.

For simplicity, the above-described cycle has been devised on the basis that the total mass of working fluid circulated during charge, m_{chg}, is precisely equal to that circulated during discharge, m_{dis}. This is not essential, provided overall "heat balance"

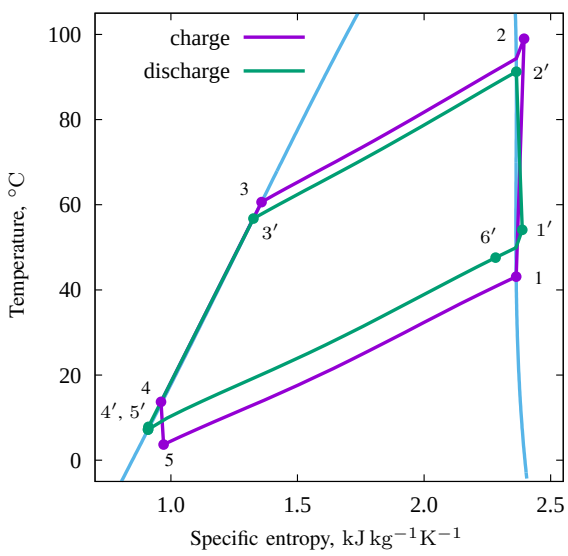

(a) *T-s* diagram

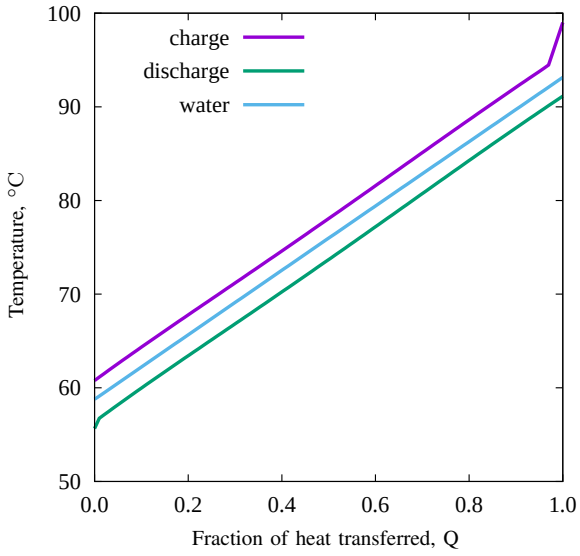

(b) *T-Q* hot HX

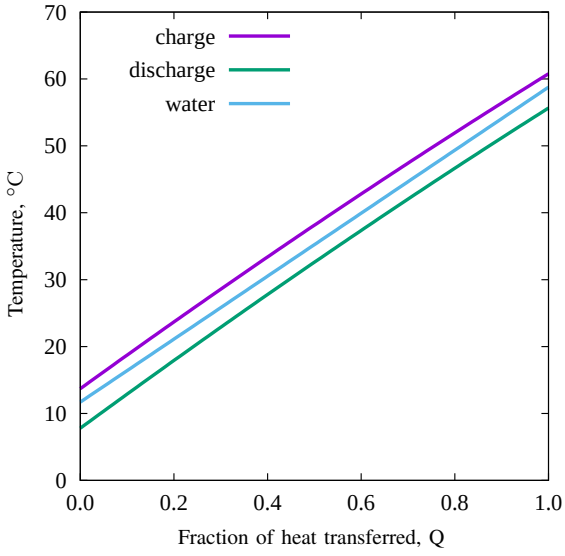

(c) *T-Q* mid HX

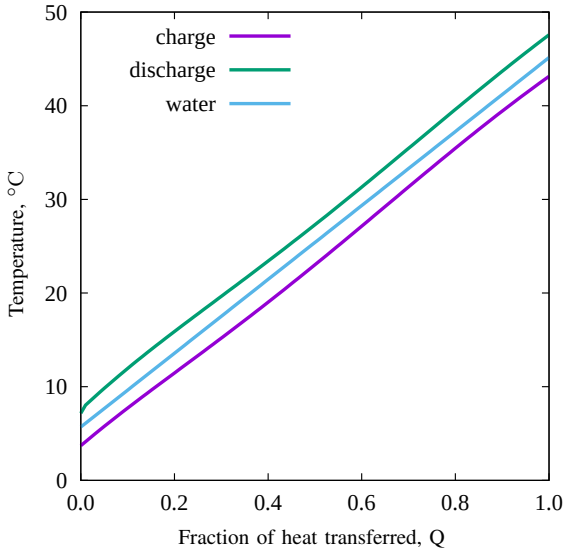

(d) *T-Q* cold HX

Fig. 8: *T-s* and *T-Q* diagrams for the baseline cycle. Primes ($'$) in (a) denote states during discharge.

is fulfilled – i.e., $m_{\mathrm{chg}}\Delta h_{\mathrm{chg}} = m_{\mathrm{dis}}\Delta h_{\mathrm{dis}}$ for all heat exchangers. Relaxing this constraint gives more flexibility in the location of the discharge state points on the *T-s* diagram and might allow for slight improvements in cycle performance.

4.2 Thermodynamic indicators

The main quantities that serve to characterise the thermodynamic performance of the system are:
(i) Round trip efficiency. This reflects how close the cycle is to being reversible and is given by

$$\eta_{\mathrm{RT}} = \frac{W_{\mathrm{dis}}}{W_{\mathrm{chg}}} = \frac{m_{\mathrm{dis}}(\{h_{2'} - h_{1'}\} - \{h_{4'} - h_{5'}\})}{m_{\mathrm{chg}}(h_2 - h_1)} \tag{6}$$

Note that a number of minor losses have been ignored, including mechanical (friction) losses, fan and circulating pump work, and motor/generator losses. Quantifying these accurately requires much more detailed design but, based on other studies [27], they might be expected to reduce the efficiency by a further 5-10%.
(ii) Energy density. This is defined as the work returned during discharge per unit tank volume, accounting for all tanks:

$$\rho_E = \frac{m_{\mathrm{dis}}(\{h_{2'} - h_{1'}\} - \{h_{4'} - h_{5'}\})}{(m_c + m_m + m_h)/\rho_w} \tag{7}$$

Table 1: Working fluid states for the baseline cycle

	State	T °C	p bar	h kJ/kg	s kJ/kg/K
Charge	1	43.1	4.57	573	2.36
	2	99.0	17.54	648	2.39
	3	60.8	17.54	284	1.36
	4	13.7	17.54	161	0.96
	5	3.7	4.57	161	0.97
Discharge	$1'$	54.1	5.60	590	2.39
	$2'$	91.1	16.26	633	2.37
	$3'$	55.7	16.26	270	1.32
	$4'$	7.8	16.26	146	0.91
	$5'$	7.2	5.60	144	0.91
	$6'$	47.6	5.60	556	2.28

Table 2: Store temperatures and water mass flows (per kg of working fluid) for the baseline case.

Water temperature (°C)	Hot store	Mid store	Cold store
Pre-charge	58.8	11.7	45.1
Post-charge	93.1	58.8	5.7
Post-discharge	58.8	11.7	45.1
HX mass flow (kg/kg)	2.52	0.63	2.50

where m_c, m_m and m_h are the masses of water in the cold, mid-temperature and hot tanks respectively. These are determined by balancing the heat capacities of the hot and cold streams in each heat exchanger. The energy density is used to estimate the footprint of the storage system and the cost per unit energy capacity.

(iii) Power density. This gives a preliminary indication of compressor and turbine size and cost. It is defined here as the power output per unit volumetric flow based on turbine exit conditions:

$$\rho_P = \rho_{1'}\{(h_{2'} - h_{1'}) - (h_{4'} - h_{5'})\} \tag{8}$$

(iv) The work ratio. As noted above, this determines the sensitivity of cycle performance to compression and expansion losses. It is given by

$$r_w = \frac{h_{2'} - h_{1'}}{h_{4'} - h_{5'}} \tag{9}$$

High work ratio also reduces the total cost of turbomachinery because feedpumps and throttles are much cheaper than compressors and turbines.

(v) Heat-to-work ratio. This is the ratio between the total (unsigned) heat transferred in all heat exchangers and the net work returned during discharge. With reference to fig. 8a,

$$\text{HWR} = \frac{(h_{2'} - h_{4'}) + (h_{1'} - h_{5'})}{(h_{2'} - h_{1'}) - (h_{4'} - h_{5'})} \tag{10}$$

The HWR provides a broad indication of the relative cost of heat exchangers. It also relates (inversely) to the energy density, ρ_E.

The above-described quantities are tabulated below for the baseline cycle (bold figures) and for two other turbomachinery efficiencies. The round-trip efficiency, although lower than some thermo-mechanical systems, is quite respectable given the inherent difficulties associated with low-temperature storage systems. As noted above, η_{RT} cannot exceed η_{is}^2 and, for all three cases, roughly 75% of this value is attained. The high work ratio and tuning of the working fluid to achieve near-parallel *T-Q* diagrams are the main factors contributing to this outcome. The high heat-to-work ratio is an inevitable consequence of low-temperature storage, but is also exacerbated by the need for recuperation – i.e., due to the temperature overlap between processes 3 to 4 and 5 to 1. (By contrast a transcritical CO_2 system has no such overlap, due to its isothermal cold side, and typically has an HWR around 7.) High HWR emphasises the need to reduce heat-exchanger losses and suggests that the heat exchangers will be a significant factor in the cost per unit *power* capacity.

The energy density is some 60% of the maximum achievable for this type of system (see section 1), the discrepancy being due to irreversibilities during discharge and there being insufficient glide to match T_1 and T_3 to the ideal T_d^*. Finally, the power density is roughly one tenth that of transcritical CO_2 cycle [11], but significantly higher values can be obtained by adjustments to the mixture composition.

The sensitivity of the main performance parameters to the nominal heat-exchange ΔT is shown in Table 4. This provides an indication of the cost-efficiency trade off since the heat-exchange area, A, scales as $1/\Delta T$. The figures reveal the diminishing

Table 3: Principal thermodynamic indicators

	$\eta_{\rm is} = 80\%$	$\eta_{\rm is} = \mathbf{85\%}$	$\eta_{\rm is} = 90\%$
Round-trip efficiency, (%)	48.5	**54.5**	61.3
Energy density ($\mathrm{kWh_e\,m^{-3}}$)	2.02	**2.20**	2.40
Power density ($\mathrm{MWs\,m^{-3}}$)	0.43	**0.47**	0.52
Work ratio	17.5	**20.7**	21.0
Heat-to-work ratio	25.3	**21.1**	20.8

returns to be gained from increased heat-exchanger costs – for example a 33% increase in *UA* (where U is overall heat transfer coefficient) yields only a 6% increase in $\eta_{\rm RT}$. In fact, reducing ΔT much below 1.5 °C with the current alkane mix is not possible due to the emergence of pinch-point problems.

Table 4: Sensitivity to heat exchanger performance

ΔT °C	*UA* relative to baseline	η_{RT} %	Energy density $\mathrm{kWh/m^3}$	Power density $\mathrm{MWs/m^3}$
1.5	1.33	57.8	2.34	0.48
2.0	**1.00**	**54.5**	**2.20**	**0.47**
4.0	0.49	41.2	1.66	0.42

4.3 Exergetic loss distribution

With the exception of the air-cooled condenser, all devices are adiabatic. Exergetic losses are therefore proportional to the entropy creation, which in turn equates to the net entropy efflux from each device. Thus, for example, the lost work associated with the charge compressor is

$$< W_L = T_0 m_{\rm chg}(s_2 - s_1) \tag{11}$$

For the air-cooled condenser the lost work occurs only during discharge and is given by

$$W_L = m_{\rm dis}(b_{1'} - b_{6'}) \tag{12}$$

where $b = h - T_0 s$ is the steady-flow availability function.

Exergetic losses for each component are given in Table 5 for the baseline cycle, expressed as a percentage of the charge work $W_{\rm chg}$. Just less than half (45%) of the loss is due to heat transfer irreversibility and the remainder is due to compression and expansion losses, including throttling. At 4% of $W_{\rm chg}$ the throttling loss is not insignificant and could, in principle, be reduced by employing a work-producing expansion device designed for two-phase applications (e.g., a twin-screw expander [28]).The air-cooled condenser loss is also quite significant (more than 10% of the total), reflecting the rejection of heat at substantially above-ambient temperature. This loss could be shifted to the charge cycle with the advantage of a slight increase in the discharge efficiency and storage density.

Table 5: Exergetic loss distribution for the baseline system. Losses are expressed as a percentage of $W_{\rm chg}$.

	Charge	Discharge	Total
Compressor / Pump	11.7	0.5	12.3
Throttle / Turbine	4.0	9.0	13.0
HX (hot)	2.6	2.6	5.1
HX (mid)	1.3	1.5	2.8
HX (cold)	3.8	3.9	7.6
Heat rejection	0.0	4.9	4.9
Total:	**23.3**	**22.2**	**45.5**

5. Preliminary cost considerations

Given the preliminary nature of this study, the cost analysis presented here is restricted to estimates of the major components of capital cost, rather than more sophisticated measures (e.g., levelised cost of storage) that depend on how the system is used, its lifetime and variations in electricity costs. The estimations presented below implicitly assume that correlations based on historical data for existing equipment can be used to estimate the cost of equivalent new equipment – i.e., development and adaption costs are not considered. This is tantamount to "n-th of a kind" (NOAK) costing and is appropriate for long-term comparisons.

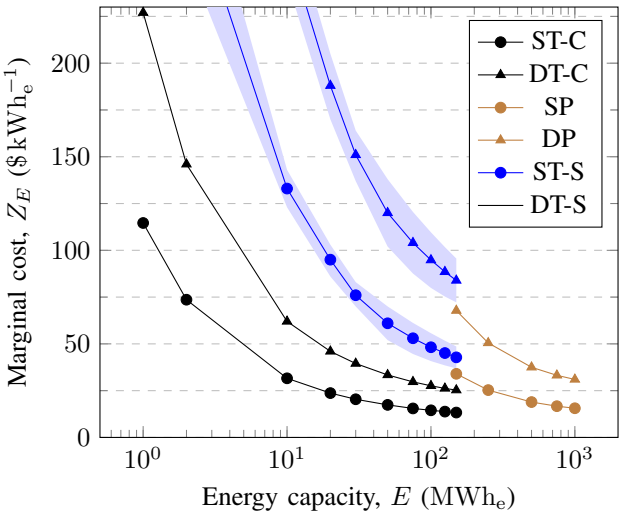

Fig. 9: Cost of energy capacity for different storage choices, with standard deviation for steel tanks. Key: ST = single tank; DT = double tank; SP = single pit; DP = double pit; -C/-S = concrete/steel.

In common with pumped hydro and most thermo-mechanical storage systems, the power- and energy-related costs of PTES may be separated, such that the total capital cost for a scheme with energy capacity E and power capacity P is given by

$$C \simeq Z_P P + Z_E E \tag{13}$$

where Z_P and Z_E are the marginal costs per unit power and per unit energy respectively. The main contributors to the first term are pumps, turbines, compressors, motor-generators and heat exchangers, whereas the second term accounts for the storage media and tanks or reservoirs.

5.1 Estimate of marginal energy cost, Z_E

The marginal cost per unit energy storage capacity is estimated from,

$$Z_E \simeq \frac{c_{\rm tnk} + c_{\rm ins}(V_{\rm ins}/V_{\rm tnk}) + c_{\rm med}}{\rho_E} \tag{14}$$

where $c_{\rm tnk}$, $c_{\rm ins}$ and $c_{\rm med}$ are the costs per unit volume of the tanks, the insulation and the storage medium (water) respectively. Water is sufficiently cheap ($\sim$ 2\$ per tonne [29]) that Z_E is dominated by the tank and insulation costs, both of which depend on the size of the system. The ratio of insulation to tank volume $(V_{\rm ins}/V_{\rm tnk})$ is determined on the basis of a simple lumped heat capacity model (see for example Appendix B of Ref. [30]) assuming a 1% heat loss per day and "square" ($H = D$) tanks. The insulation is assumed to be glass wool, for which $c_{\rm ins} \sim 100\$\,{\rm m}^{-3}$ and $\lambda = 0.038{\rm W\,m^{-1}K^{-1}}$. Typically, insulation costs constitute around 0.1% of Z_E, but would increase in inverse proportion to the specified percentage heat loss per day.

The purchased-equipment cost of the tanks is estimated from correlations available in the literature. For example, for carbon steel tanks of the "floating roof" type (designed to deal with situations with significant vapour pressure), one correlation takes the form [31]

$$c_{\rm tnk} = 12,586 V_{\rm tnk}^{-0.49} \quad \$\,{\rm m}^{-3} \tag{15}$$

Several other correlations are available for similar steel tanks [32]–[34], for concrete tanks [35] and for excavated pits [23]. Details of these correlations are given in the supplementary information. In all cases the chemical engineering cost index (CECI) is applied to update costs to a 2018 \$ basis, and an additional multiplier of 1.4 (see Ref. [35]) is applied to the tank correlations to estimate the total installed cost (e.g., to account for foundations) and provide a fairer comparison with pits.

Figure 9 shows the resulting marginal energy cost Z_E as a function of energy capacity E, highlighting the economies of scale. (Note that E is determined on the basis of energy delivered and thus accounts for losses during discharge.) The shaded region for steel tanks reflects the spread from different correlations. As expected, single-tank/pit systems are approximately half the cost of double tanks, but would require some means of isolating the hot and cold fluid for longer-term storage. Single concrete tanks provide the cheapest option at around 13 \$/kWh$_e$ for $E = 150\,{\rm MWh_e}$ capacity, followed by excavated pits at 16 \$/kWh$_e$ for 1 GWh$_e$ capacity. Concrete vessels would probably require internal insulation in order to avoid damage from thermal cycling, which may raise the cost. Finally, the cheapest estimates for steel tanks are around 40-45 \$/kWh$_e$, but these tanks perhaps have the best scope for operating at higher temperatures, which would increase ρ_E and lower Z_E.

5.2 Estimate of marginal power cost, Z_P

In order to benefit from the low marginal energy costs described above (and recognising that unit power costs are likely to be high due to the high HWR and low power density), Z_P is estimated for a nominal design with $100\,\mathrm{MWh_e}$ / $5\,\mathrm{MW}$ capacity (i.e., with $20\,\mathrm{hrs}$ discharge duration). McTigue *et al.* [27] present a compilation of cost correlations of process equipment often employed in PTES systems, many of which are also used in this work. In particular, cost correlations for compressors and turbines are taken from Refs. [12], [35]–[37], for pumps from [10], [34], [38], for motors and generators from [10], [39] and for plate heat exchangers from [10], [40]. (Full details of these cost correlations are shown in the supplementary information.) The resulting minimum and maximum contributions to Z_P are tabulated below, together with basic sizing data for each component.

Table 6: Main contributions to marginal power cost, Z_P.

	Size	Cost, \$k		\$/kW$_e$	
		Min	Max	Min	Max
Compressor	9.2 MW	75	2,300	15	459
Turbine	5.3 MW	88	1,670	18	334
Pump	0.3 MW	36	212	7	43
Motor-generator	9.2 MW	1,170	2,390	235	477
HX (hot)	20,000 m^2	1,770	2,700	355	539
HX (mid)	12,000 m^2	1,140	1,770	228	354
HX (cold)	25,000 m^2	2,080	3,140	416	628
Air cooled HX	1,500 m^2	209	347	42	69
Total (to 2 s.f.)				**1,300**	**2,900**

It is striking that the estimated costs span a very broad range for some components – notably compressors, pumps and turbines – and a few explanatory comments are in order. The simplest correlations for turbomachinery depend only on the power rating, and give per kW costs at the top end of the range. This is clearly a simplification because the cost of a compressor, for example, will depend on its type, the number of stages and the volumetric flow rate. This is recognised in the other correlations which are rooted in Ref. [37] and which scale compressor costs as $\dot{m}\beta \ln \beta$, where β is the pressure ratio. These correlations give per kW costs that would appear unrealistically low. The most likely explanation for this is that these correlations were validated for somewhat larger-scale gas turbine compressors. Ultimately, reliable cost estimates are only possible once specific devices have been identified (see section 6 below).

Although heat exchanger cost estimates show a much narrower range, this is contingent upon achieving certain levels of overall heat transfer coefficient, U – namely averages of 1000 and $500\,\mathrm{W\,m^{-2}K^{-1}}$ for the two-phase and single-phase devices respectively and $200\,\mathrm{W\,m^{-2}K^{-1}}$ for the air-cooled condenser. Heat transfer coefficients in two-phase flows may vary very significantly as the mixture changes from all liquid to all gas and *vice versa*. The average values assumed here should be achievable based on *correlations* presented in Ref. [41] (for hydrocarbon mixtures) and in Ref. [42] (for single-phase flow in corrugated-plate heat exchangers). However, determining these heat transfer coefficients is not an area that is easily amenable to analysis as they will depend on composition, the level of mixing, the type of heat exchanger and the pressure drop. The real/actual heat transfer coefficient would need to be determined experimentally in a representative heat exchange test rig.

6. Perspectives and practicalities

6.1 Strategies for reducing costs

Given the uncertainties discussed above, it is prudent to adopt a conservative approach to costs, based on the top of the ranges, namely $Z_P \simeq 2,900\,\$/\mathrm{kW_e}$ and $Z_E \simeq 45\,\$/\mathrm{kWh_e}$. On this basis, the specified design ($20\,\mathrm{hrs}$ storage) would have an overall (as opposed to marginal) cost of $190\,\$/\mathrm{kWh_e}$. For comparison, a recent US National Renewable Energy Laboratory report on photovoltaic systems [43] gives raw (lithium-ion) battery costs of $209\,\$/\mathrm{kWh_e}$, plus additional system costs (inverter and other hardware) that bring the total purchased-equipment cost to around $275\,\$/\mathrm{kWh_e}$ for a 4-hour, utility scale system. Based on the (highest) cost estimates, the present system would break even with batteries at around $12\,\mathrm{hrs}$ capacity, with the relative benefit clearly increasing with discharge duration – e.g., for two-day capacity the *total* cost would fall to around $105\,\$/\mathrm{kWh_e}$.

Aside from batteries there are of course many other storage systems that any new technology would need to compete with. For instance, there is increasing interest in electro-thermal energy storage (ETES), in which the charging phase is achieved by direct electrical (Joule) heating. Okazaki [44], for example, discusses ETES systems using steam plant with molten-salt thermal storage, providing estimated capital costs of $800\,\$/\mathrm{kW_e}$ and $20\,\$/\mathrm{kWh_e}$ respectively. (The source publication for the latter [45] quotes a range of 11 to $19\,\$/\mathrm{kWh}$ *thermal* which would translate to around 28 to 48 $\$/\mathrm{kWh_e}$ at 40% steam plant efficiency, but this is dated 2013.) If these figures are correct then the PTES system described herein would struggle to compete on capital cost alone, but it is noted that ETES is unlikely to achieve a round-trip efficiency above 40% and that this would require large scale plant (limited by LP turbine performance) at storage temperatures in excess of $600\,^\circ\mathrm{C}$. Furthermore, various strategies might be adopted to reduce costs of the present system, including:

1. The working fluid composition could be adjusted to reduce the pressure ratio (currently 3.8) so that compression can be achieved with a single centrifugal stage. Power density also tends to increase when this is done.
2. Alternatively, at the expense of reduced efficiency, a single, "reversible" device might be used, such as a twin-screw compressor/expander.
3. Also at the expense of efficiency, smaller heat exchangers with a larger ΔT can be adopted.
4. The storage density could be increased by using an alternative storage fluid or slightly pressurising the storage tanks. As shown in the Appendix, ρ_E rises rapidly with the top temperature.

6.2 Practical considerations

Against the above list of potential improvements, it is recognised that a number of practical challenges would need to be addressed for a glide-based PTES system and some more detailed modelling is also required. For example:

1. It has been assumed in the cycle calculations that thermodynamic equilibrium is maintained during phase transition. This will require a high level of mixing which in turn may incur significant pressure losses.
2. The work required to pump the storage fluid also needs to be taken into account. Initial estimates based on heat transfer and pressure loss correlations presented in Ref. [46] suggest this would not exceed 0.2% of the turbine work, but this really needs to be considered in conjunction with the heat-exchanger costs.
3. Heat transfer coefficients and the performance of compressors and expanders with multi-component fluids is not well documented. The compressor and turbine may, for example, need a margin of superheat at inlet to avoid damage.
4. The safety implications of working-fluid flammability need to be considered. In this respect, however, it is worth noting that some hydrocarbons are already accepted refrigerants – e.g., propane is R290.
5. Off-design operation of the cycle components ultimately needs to be considered. For instance, the performance of the air-cooled condenser (once a particular design is chosen) will be influenced by the ambient temperature.

These considerations, together with the cost-reduction strategies, point to the need for an optimisation that explores the trade off between efficiency and cost, whilst simultaneously respecting the various practical constraints. This is the subject of ongoing work.

7. Conclusions

A novel form of pumped thermal energy storage has been presented, which exploits the temperature glide of zeotropic fluid mixtures. Preliminary thermodynamic design calculations have been undertaken, in conjunction with initial capital cost estimates, from which the following conclusions emerge:

1. By optimising the composition of a blend of four alkanes (ethane to pentane) it is possible to obtain a working fluid that has near-constant effective heat capacity in the two-phase region. This enables exergetically efficient heat exchange with a constant c_p storage fluid whilst also preserving the advantage of high work ratio, characteristic of Rankine cycles.
2. For the low-temperature storage system presented, using unpressurised water as the storage medium, the computed (thermodynamic) round-trip efficiency is 54.5% based on turbomachinery isentropic efficiencies of 85% and a ΔT of $2\,^{\circ}\mathrm{C}$ in the main heat exchangers. Mechanical, electrical and other minor losses are likely to take this down to around 50% or below, but no optimisation has yet been undertaken.
3. The corresponding estimates for capital cost for power and energy capacity are in the ranges 1,300–2,900 $\$/\mathrm{kW_e}$ and 15–45 $\$/\mathrm{kWh_e}$ for a nominal design of $5\,\mathrm{MW_e}$ and 20 hours discharge duration. Based on the most pessimistic of these figures, the system would break even with batteries at around 12 hours storage capacity.
4. The storage density is low (although roughly four times that of typical pumped hydro storage) thereby requiring a large footprint for long-duration systems – e.g., the nominal $100\,\mathrm{MWh_e}$ design would occupy of the order of one hectare. This is to be expected for a low-temperature system, but it is exacerbated by the need for both hot and cold storage. However, other storage media (with larger temperature separations) could in principle be used in conjunction with the same cycle.

Finally, it is noted that compared to some other forms of thermo and mechanical energy storage (e.g., compressed air and pumped hydro), the system presented here is much less restricted by geographical location, whilst its low temperature range and modest operating pressures mean that inexpensive low-carbon steels can be employed for all equipment, together with conventional gasket seals.

Credit authorship contribution statement

Antoine Koen: conceptualisation, methodology, software, investigation, formal analysis, writing; Pau Farres-Antunez: methodology, review and editing, supervision; James Macnaghten: conceptualisation, review and editing; Alexander White: review and editing, formal analysis, supervision, project administration.

Funding

The first author (AJK) was in receipt of a UK Engineering and Physical Sciences Research Council (EPSRC) studentship. The second author (PFA) was partially funded on EPSRC projects EP/P004709/1 and EP/P021867/1. All authors gratefully acknowledge the EPSRC for their support.

NOMENCLATURE

Acronyms

CAES	Compressed air energy storage
CHE	Cyclic heat engine
CHP	Cyclic heat pump
HWR	Heat-to-work ratio
HX	Heat exchanger
LAES	Liquid air energy storage
ORC	Organic Rankine cycle
PTES	Pumped thermal energy storage
RSD	Relative standard deviation

Symbols

η_{is}	Isentropic efficiency
η_{RT}	Round-trip efficiency
ρ	Density ($\mathrm{kg/m^3}$)
ρ_E	Energy density ($\mathrm{kWh_e/m^3}$)
ρ_P	Power density ($\mathrm{MW\,s/m^3}$)
σ	Standard deviation in c_p ($\mathrm{J/kg/K}$)
c_p	Isobaric specific heat capacity ($\mathrm{J/kg/K}$)
f	Mass fraction in hot storage
h	Specific enthalpy ($\mathrm{J/kg}$)
r_w	Work ratio
s	Specific entropy ($\mathrm{J/kg/K}$)
T_0	Ambient temperature, (288 K)
W	Work transfer (J)
Z_E	Marginal energy capacity cost ($\$/\mathrm{kWh_e}$)
Z_P	Marginal power capacity cost ($\$/\mathrm{kW_e}$)

Subscripts

c	cold
h	hot
chg	charge
dis	discharge
sf	storage fluid
wf	working fluid

Other symbols are defined in the text where they are used.

REFERENCES

[1] H. Anuta, P. Ralon, M. Taylor, Renewable Power Generation Costs in 2018, Tech. rep., International Renewable Energy Agency (2019).
URL https://www.irena.org/-/media/Files/IRENA/Agency/Publication/2019/May/IRENA_Renewable-Power-Generations-Costs-in-2018.pdf

[2] Lazard, Lazard's Levelized Cost of Energy Analysis - Version 14.0, Tech. rep., Lazard (2020).
URL https://www.lazard.com/perspective/levelized-cost-of-energy-and-levelized-cost-of-storage-2020/

[3] UK Government National Statistics, DUKES chapter 6: statistics on energy from renewable sources, Tech. rep., Department for Business, Energy and Industrial Strategy (2020).
URL https://www.gov.uk/government/statistics/renewable-sources-of-energy-chapter-6-digest-of-united-kingdom-energy-statistics-dukes

[4] GridWatch, Great Britain National Grid Status (2021).
URL https://www.gridwatch.templar.co.uk/index.php

[5] D. R. MacFarlane, P. V. Cherepanov, J. Choi, B. H. Suryanto, R. Y. Hodgetts, J. M. Bakker, F. M. F. Vallana, A. N. Simonov, A roadmap to the ammonia economy, Joule doi:10.1016/j.joule.2020.04.004.

[6] X. Zhang, M. He, Y. Zhang, A review of research on the Kalina cycle, Renewable and Sustainable Energy Reviews 16 (7) (2012) 5309–5318. doi:10.1016/j.rser.2012.05.040.

[7] J. Howes, Concept and development of a pumped heat electricity storage device, Proceedings of the IEEE 100 (2) (2012) 493–503. doi:10.1109/JPROC.2011.2174529.

[8] B. R. Bollinger, Malta Pumped Heat Electricity Storage (PHES) for Coal Exit and Energy Transition from Fossil to Renewable Energies, in: 2nd International Workshop on Carnot Batteries, Stuttgart, Germany, 2020, pp. 1–15.

[9] W. Steinmann, The CHEST (Compressed Heat Energy STorage) concept for facility scale thermo mechanical energy storage, Energy 69 (2014) 543–552. doi:10.1016/J.ENERGY.2014.03.049.
URL https://www.sciencedirect.com/science/article/pii/S0360544214003132

[10] M. Morandin, M. Mercangöz, J. Hemrle, F. Maréchal, D. Favrat, Thermoeconomic design optimization of a thermo-electric energy storage system based on transcritical co2 cycles, Energy 58 (2013) 571–587. doi:10.1016/j.energy.2013.05.038.

[11] A. Koen, P. Farres Antunez, A. White, A study of working fluids for transcritical pumped thermal energy storage cycles, in: 2019 Offshore Energy and Storage Summit, OSES 2019, 2019, pp. 1–7. doi:10.1109/OSES.2019.8867217.

[12] P. Farres Antunez, Modelling and development of thermo-mechanical energy storage, Ph.D. thesis, University of Cambridge (2019). doi:10.17863/CAM.38056.

[13] A. White, G. Parks, C. N. Markides, Thermodynamic analysis of pumped thermal electricity storage, Applied Thermal Engineering 53 (2) (2013) 291–298. doi:10.1016/J.APPLTHERMALENG.2012.03.030.

[14] R. B. Laughlin, Pumped thermal grid storage with heat exchange, Journal of Renewable and Sustainable Energy 9 (4) (2017) 044103. doi:10.1063/1.4994054.

[15] O. J. Demuth, Analyses of mixed hydrocarbon binary thermodynamic cycles for moderate temperature geothermal resources, Tech. Rep. CONF-810812-42, EG and G Idaho, Inc., Idaho Falls (USA) (1 1981).
URL https://www.osti.gov/biblio/5598742-analyses-mixed-hydrocarbon-binary-thermodynamic-cycles-moderate-temperature-geothermal-resources

[16] R. Murugan, P. Subbarao, Thermodynamic Analysis of Rankine-Kalina Combined Cycle, International Journal of Thermodynamics 11 (3) (2008) 133–141.
URL https://dergipark.org.tr/ijot/issue/5769/76761

[17] O. A. Oyewunmi, C. N. Markides, Thermo-economic and heat transfer optimization of working-fluid mixtures in a low-temperature organic Rankine cycle system, Energies 9 (6). doi:10.3390/en9060448.

[18] T. Zhang, X. Zhang, X. Xue, G. Wang, S. Mei, Thermodynamic analysis of a hybrid power system combining kalina cycle with liquid air energy storage, Entropy 21 (3) (2019) 220.

[19] M. Soltani, M. H. Nabat, A. R. Razmi, M. Dusseault, J. Nathwani, A comparative study between orc and kalina based waste heat recovery cycles applied to a green compressed air energy storage (caes) system, Energy Conversion and Management 222 (2020) 113203.

[20] X. Wang, L. Zhao, Analysis of zeotropic mixtures used in low-temperature solar rankine cycles for power generation, Solar Energy 83 (5) (2009) 605–613.

[21] L. Zhao, J. Bao, Thermodynamic analysis of organic rankine cycle using zeotropic mixtures, Applied Energy 130 (2014) 748–756.

[22] T. Eller, F. Heberle, D. Brüggemann, Second law analysis of novel working fluid pairs for waste heat recovery by the kalina cycle, Energy 119 (2017) 188–198.

[23] Energinet, Technology Data for Energy storage, Tech. rep., Danish Energy Agency (2019).
URL https://www.solarthermalworld.org/sites/default/files/news/file/2019-05-17/technology_data_catalogue_for_energy_storage.pdf

[24] J. Erik Nielsen, P. Per Alex Sørensen, P. Guido Bakema, P. Egermann, S. Charlotte Rey, S. Charles Maragna, B. Virginie Hamm, F. Hahn, G. Isabella Nardini, G. Joris Koornneef, T. Knud Dideriksen, HEATSTORE Underground Thermal Energy Storage (UTES) - state-of-the-art, example cases and lessons learned, Tech. rep., Geothermica (2019).
URL https://www.solarthermalworld.org/sites/default/files/news/file/2019-05-17/heatstore_utes_state_of_the_art_wp1_d1.1_final_2019.04.26.pdf

[25] E. W. Lemmon, , I. H. Bell, M. L. Huber, M. O. McLinden, NIST Standard Reference Database 23: Reference Fluid Thermodynamic and Transport Properties-REFPROP, Version 10.0, National Institute of Standards and Technology (2018). doi:10.18434/T4/1502528.

[26] O. Kunz, W. Wagner, The gerg-2008 wide-range equation of state for natural gases and other mixtures: an expansion of gerg-2004, Journal of chemical & engineering data 57 (11) (2012) 3032–3091. doi:10.1021/je300655b.

[27] J. D. McTigue, P. Farres-Antunez, K. Sundarnath Jawaharlal Ayyanathan, C. N. Markides, A. J. White, Techno-economic analysis of recuperated Joule-Brayton pumped thermal energy storage, submitted to Applied Energy.

[28] G. Bianchi, S. Kennedy, O. Zaher, S. A. Tassou, J. Miller, H. Jouhara, Numerical modeling of a two-phase twin-screw expander for trilateral flash cycle applications, International Journal of Refrigeration 88 (2018) 248–259. doi:10.1016/j.ijrefrig.2018.02.001.

[29] Anglian Water, Standard Rates (2019).
URL https://www.anglianwater.co.uk/account-and-bill/tariffs-and-charges/standard-rates/

[30] A. J. White, J. D. McTigue, C. N. Markides, Analysis and optimisation of packed-bed thermal reservoirs for electricity storage applications, Proceedings of the Institution of Mechanical Engineers, Part A: Journal of Power and Energy 230 (7) (2016) 739–754. doi:10.1177/0957650916668447.

[31] W. D. Seider, J. D. Seader, D. R. Lewin, Widagdo, Product and Process Design Principles, Synthesis, Analysis, and Evaluation, 3rd Edition, John Wiley & Sons, 2010.

[32] R. Turton, J. A. Shaeiwitz, D. Bhattacharyya, W. B. Whiting, Analysis, Synthesis, and Design of Chemical Processes, 5th Edition, Prentice Hall, 2018.

[33] J. M. Coulson, J. F. Richardson, R. K. Sinnott, Chemical engineering design, 4th Edition, Elsevier, 2005.

[34] M. Peters, K. Timmerhaus, R. West, Plant design and economics for chemical engineers, 5th Edition, Boston, Boston, 2003.

[35] J. Couper, R. Penney, J. Fair, S. Walas, Chemical process equipment : selection and design, 3rd Edition, Waltham, MA, 2012.

[36] Black, Veatch, Cost and Performance data for Power Generation Technologies, Tech. rep., Black and Veatch (2012).

[37] A. Agazzani, A. Massardo, A tool for thermoeconomic analysis and optimization of gas, steam, and combined plants, Journal of Engineering for Gas Turbines and Power 119 (4) (1997) 885–892. doi:10.1115/1.2817069.

[38] H. P. Loh, J. Lyons, C. W. White, Process Equipment Cost Estimation Final Report, Tech. rep., National Energy Technology Laboratory (2002). doi:10.2172/797810.

[39] A. Benato, A. Stoppato, Integrated Thermal Electricity Storage System: Energetic and cost performance, Energy Conversion and Management 197 (2019) 111833. doi:10.1016/J.ENCONMAN.2019.111833.

[40] Z. Guo-Yan, W. En, T. Shan-Tung, Techno-economic study on compact heat exchangers, International journal of energy research 32 (12) (2008) 1119–1127. doi:10.1002/er.1449.

[41] Y. Samokhvalov, A. Kolesnikov, A. Krotov, A. Parkin, E. S. Navasardyan, I. Arkharov, Heat transfer in the structure of a spiral-wound heat exchanger for liquefied natural gas production: review of numerical models for the heat-transfer coefficient of condensation for a hydrocarbon mixture in a horizontal tube, Journal of Enhanced Heat Transfer 25 (2). doi:10.1615/JEnhHeatTransf.2018026396.

[42] T. M. Abou Elmaaty, A. Kabeel, M. Mahgoub, Corrugated plate heat exchanger review, Renewable and Sustainable Energy Reviews 70 (2017) 852–860. doi:10.1016/j.rser.2016.11.266.

[43] R. Fu, T. W. Remo, R. M. Margolis, 2018 US utility-scale photovoltaics-plus-energy storage system costs benchmark, Tech. rep., National Renewable Energy Lab.(NREL), Golden, CO (United States) (2018). doi:10.2172/1483474.

[44] T. Okazaki, Electric thermal energy storage and advantage of rotating heater having synchronous inertia, Renewable Energy 151 (2020) 563–574.

[45] M. Jonemann, Advanced thermal storage system with novel molten salt: December 8, 2011-april 30, 2013, Tech. rep., National Renewable Energy Lab.(NREL), Golden, CO (United States) (2013).

[46] W. M. Kays, A. L. London, Compact heat exchangers.

APPENDIX: DERIVATION OF MAXIMUM ρ_E

The expression for ρ_E given in section 1 (Eq.2) may be rearranged in the form

$$\rho_E = \rho_w c_{pw}(f\{T_h - T_c\} + T_c - T_d) \tag{16}$$

The hot and cold temperatures are assumed fixed, so optimising the energy density is a matter of choosing the common discharged temperature T_d and mass distribution f that maximise ρ_E. Differentiating eq.(16) with respect to T_d and setting to zero in the usual fashion gives

$$(T_h - T_c)\frac{\mathrm{d}f}{\mathrm{d}T_d} - 1 = 0 \tag{17}$$

The relationship between f and T_d is determined by noting that the system entropy remains constant (see discussion in section 1). Thus (per unit mass),

$$\Delta s = c_{pw}\left(f \ln\frac{T_d}{T_h} + \{1-f\}\ln\frac{T_d}{T_c}\right) = 0 \tag{18}$$

Substituting into eq.(17) gives after straightforward manipulation

$$T_d^* = \frac{T_h - T_c}{\ln(T_h/T_c)} \tag{3}$$

where the * denotes the optimal condition. The optimal mass distribution is obtained by rearranging eq.(18) with $T_d = T_d^*$:

$$f^* = \frac{\ln(T_d^*/T_c)}{\ln(T_h/T_c)} \tag{4}$$

Finally, the maximum energy density is given in normalised form as

$$\phi^* = \frac{\rho_E^*}{\rho_w c_{pw} T_c} = f^*\left(\frac{T_h}{T_c} - 1\right) + 1 - \frac{T_d^*}{T_c} \tag{19}$$

Figure 10 shows f^* and ϕ^* plotted as functions of the ratio T_h/T_c. It is clear that (i) the optimum mass distribution remains close to an equal split between the hot and cold tanks and (ii) rapid improvements in energy density would be gained by operating at higher temperatures.

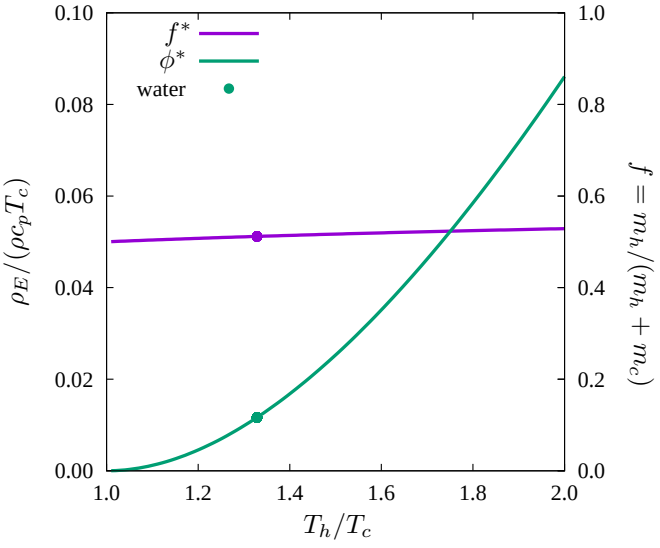

Fig. 10: Optimum mass distribution between tanks and normalised energy density. The symbols correspond to water at atmospheric pressure ($T_c = 4°\mathrm{C}$, $T_h = 96°\mathrm{C}$).